Progress In Electromagnetics Research B, Vol. 72, 149–168, 2017

Retrieval of Major Greenhouse Gas Profiles with LEO-Ground Infrared Laser Occultation (LGIO) Technique

Mu-Min Chiou and Jean-Fu Kiang*

Abstract—A LEO-ground infrared laser occultation (LGIO) technique is proposed to retrieve the greenhouse gas (GHG) profiles around a specific location, including the analysis of key factors and practical issues that may affects its efficacy. A harmony search with ensemble consideration (HS-EC) algorithm is applied to retrieve the volume mixing ratio (VMR) profiles of H_2O and three major GHGs, CO_2, CH_4 and N_2O. The vertical resolution of retrieved GHG profiles is 1 km from ground level up to 20 km at height. The errors in VMR of H_2O, CH_4, N_2O and CO_2 are below 10, 5, 5 and 3%, respectively, up to 45 km above ground.

1. INTRODUCTION

Radio occultation (RO) technique was applied to retrieve the refractivity profile in the Earth atmosphere, by applying Abel transform to the Global Positioning System (GPS) signals received at low-earth-orbit (LEO) satellites [1]. In [2], a LEO-LEO microwave occultation (LMO) technique was applied to retrieve the pressure, temperature and humidity profiles, with radio signals at 8–30 GHz and 175–200 GHz [3]. A LEO-LEO infrared laser occultation (LIO), operating in the short-wave infrared (SWIR) spectrum of 2–2.5 μm, was applied to retrieve profiles of water vapor (H_2O), carbon dioxide (CO_2) and methane (CH_4) in the upper troposphere and lower stratosphere (UTLS), 5–35 km above ground, as well as ozone (O_3) from 10 km above [4].

The root-mean-square (rms) error in retrieving the greenhouse gas (GHG) profiles was on the order of 1–3%, at a vertical resolution of 1 km under clear-air conditions (without clouds or turbulence) [4]. These retrieval techniques were based on the differential transmission derived from the data in a pair of channels carefully selected for each target species.

The LMO and LIO techniques were combined to implement a LEO-LEO microwave and infrared-laser occultation (LMIO) technique, which was capable of retrieving the profiles of air pressure, water-vapor pressure, temperature and greenhouse gases more effectively [2, 5]. In [6], a GHG retrieval algorithm was proposed to remove cloud and turbulence effects embedded in the infrared-laser transmissions.

The profiles obtained by applying space-based occultation techniques have a typical horizontal resolution of 200–300 km along the occultation path [7], and are less accurate in the lower troposphere, especially when a super-refractive (SR) layer exists [8], which occurs quite often in maritime areas [9]. In addition, it is difficult to plan a mission for any specific region over a specific time period [10].

Ground-based GPS radio occultation techniques, with a receiver placed near the Earth's surface [10, 11], were proposed for regional weather and climate studies [10, 12]. The Abel transform, generally used in space-borne radio occultation techniques, is not applicable to ground-based RO technique, because the latter may not be capable of receiving signals coming at negative elevation

Received 7 November 2016, Accepted 5 January 2017, Scheduled 24 January 2017

* Corresponding author: Jean-Fu Kiang (jfkiang@ntu.edu.tw).

The authors are with the Department of Electrical Engineering and The Graduate Institute of Communication Engineering, National Taiwan University, Taipei 106, Taiwan, R.O.C..

angles [12, 13]. The Abel transform requires the signals to traverse the atmosphere over the tangent point, which is the point along a ray path nearest to the ground. Studies have been conducted to explore the feasibility and limitation of using a ground-based GPS receiver to retrieve profiles of atmospheric properties. The refractivity profile was retrieved by applying a ray-tracing method to fit the measured tropospheric delays of GPS data [12, 13]. In [13], a three-level model was proposed to characterize the ducting conditions near coast, in which two constant refractivity gradients and another fixed refractivity gradient of -160 N-unit/km were assumed. An exhaustive search method was proposed, with the retrieval altitude ranging from the boundary layer to 10 km above ground, to compensate for the effect of constant refractive gradients [12]. The vertical resolution was 1 km and the refractivity error was 3%, with deviation smaller than 10 N-units.

In this work, a LEO-ground infrared laser occultation (LGIO) technique is proposed to retrieve profiles of H_2O and major GHGs around a specific receiver site. Simlar to the conventional space-based LIO techniques [4], the atmosphere is assumed to be free from clouds and aerosols in this work. Defocusing, Rayleigh scattering and absorption by GHG trace species are the main factors to reduce the signal intensity. The absorption effects of H_2O on the accuracy of target differential transmission at low altitudes are considered. Then, three GHGs less affected by H_2O are selected out of six species and four isotopes originally demonstrated in a space-based LIO technique [4]. A harmony search with ensemble consideration (HS-EC) algorithm [14, 15] is applied to retrieve the profiles of these three species and H_2O.

This paper is organized as follows. The calculation of transmission in the LGIO technique and relevant considerations are presented in Section 2. The harmony search algorithm for retrieving GHG profiles is presented in Section 3, and the key factors that determine the accuracy of the retrieved VMR profiles are analyzed in Section 4. In Section 5, the VMR profiles of H_2O and these three GHGs at three different latitudes are retrieved by simulations, and the plausibility of monitoring diurnal CO_2 profile is also demonstrated. Finally, some conclusions are drawn in Section 6.

2. TRANSMISSION IN LEO-GROUND INFRARED LASER OCCULTATION

Figure 1 shows the geometry of ray path in a ground-based radio occultation scenario, assuming that the atmospheric properties depend only on r. Rx and Tx represent an infrared receiver on the ground and a LEO satellite, respectively, at distances of r_1 and r_2, respectively, from the Earth center. A point along the ray path is labeled with the radial distance r and the angle ϕ measured from the local zenith.

To trace a ray path, the atmosphere below the height of Tx is modeled as a stack of thin layers, with the refractive index in each layer approximated as a linear function of height. A ray path is launched from Tx with an initial angle $\phi = \phi^{(0)}$. Subsequent segments of the ray path in the layers below Tx are determined by imposing the Bouger's law, $a = nr\sin\phi$, in the order of descending height, where a is the impact parameter of this ray path and n is the refractive index. If the intersection point of the lowest segment lies above (below) Rx, $\phi^{(0)}$ will be incremented (decremented) to $\phi^{(1)}$, based on which another

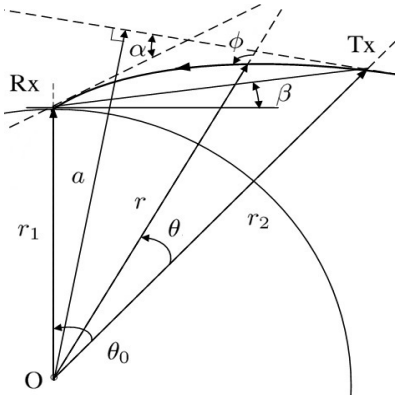

Figure 1. Geometry of ray path in a ground-based radio occultation scenario.

ray path is launched. The iteration process continues until the intersection point falls sufficiently close to Rx.

The refractivity, $N = 10^6 \times (n-1)$ (in N-unit), in the IR band can be empirically expressed as [16]

$$N(h) = \left(c_1 + \frac{c_2}{d_1 - 1/\lambda'^2} + \frac{c_3}{d_2 - 1/\lambda'^2}\right) \frac{P(h)}{T_0(h)} - c_4 P_w(h) \tag{1}$$

where $T_0(h)$ (K) is the temperature; $P(h)$ (hPa) and $P_w(h)$ (hPa) are the atmospheric pressure and water-vapor pressure, respectively; λ' (μm) is the IR wavelength; the empirical coefficients are $c_1 = 23.7104$ (K/hPa), $c_2 = 6839.34$ (K/hPa/μm^2), $c_3 = 45.473$ (K/hPa/μm^2), $d_1 = 130$ (μm^{-2}), $d_2 = 38.9$ (μm^{-2}) and $c_4 = 0.038$ (hPa^{-1}). The profiles of pressure, temperature and humidity can be retrieved by applying a ground-based RO technique [12] to weather forecast data such as the European Centre for Medium-Range Weather Forecasts (ECMWF) data [17]. Alternatively, these profiles can be simulated with the FASt Atmospheric Signature CODE (FASCODE) atmospheric model [18].

2.1. Transmission along a Ray Path

The loss due to gas absorption along a ray path can be calculated by applying the Bouguer-Lambert-Beer law [19]

$$I = I_0 e^{-\tau} = I_0 \times 10^{T/10} \tag{2}$$

where I and I_0 are the intensities (in W/m^2/sr) at Rx and Tx, respectively; $T = 10 \log_{10} e^{-\tau}$ is the transmission (in dB); τ is the optical thickness along the ray path between Tx and Rx, which is determined as

$$\tau = \int_{\mathrm{Tx}}^{\mathrm{Rx}} k d\ell \tag{3}$$

where $k = \rho\kappa$ (1/m) is the absorption coefficient [20], and ρ (kg/m^3) and κ (m^2/kg) are the mass density and mass absorption coefficient, respectively. The mass absorption coefficients can be determined by using the line parameters in the HITRAN database [21], along with the profiles of pressure, temperature and molecular composition in the atmosphere.

By using Eq. (3) to compute τ along the ray path, with $d\ell = \sqrt{dr^2 + r^2 d\theta^2} = dr/\cos\phi$, then transforming τ to T by using Eq. (2), we have

$$T(\beta) = 10 \log_{10} \exp\left\{-\int_{x_1}^{x_2} k(x) \frac{x}{\sqrt{x^2 - a^2}} \frac{dr}{dx} dx\right\} \tag{4}$$

where $x = nr$ is called the refractional radius [12], and x_1 and x_2 are the refractional radii at Rx and Tx, respectively. The absorption coefficient above the top-of-atmosphere (TOA), which is 70 km above ground for LIO signals, is approximated as zero [2].

Referring to Figure 1, the bending angle is determined as

$$\alpha = \int_{\mathrm{Rx}}^{\mathrm{Tx}} \frac{d\ell}{r_c}$$

where r_c is the radius of the curvature of the ray path, which is calculated as

$$r_c = \frac{\left[r^2 + (dr/d\theta)^2\right]^{3/2}}{r^2 + 2(dr/d\theta)^2 - r(d^2r/d\theta^2)}$$

Hence, the bending angle can be represented as

$$\alpha = -a \int_{r_1}^{r_2} \frac{dn/dr}{n\sqrt{r^2 n^2 - a^2}} dr = -a \int_{x_1}^{x_2} \frac{dn/dx}{n\sqrt{x^2 - a^2}} dx$$

which is a function of the impact parameter a of the ray path [13]. The spherical angle between RX and Tx is determined as

$$\theta_0 = \sin^{-1} \frac{a}{x_1} - \sin^{-1} \frac{a}{x_2} + \alpha$$

Given the positions of Tx and Rx, the angle θ_0 between $\overline{\text{OTx}}$ and $\overline{\text{ORx}}$ is determined geometrically, and the elevation angle β is related to θ_0 as

$$\beta = \tan^{-1} \frac{r_2 \cos\theta_0 - r_1}{r_2 \sin\theta_0}$$

which is used to label the transmission along the ray path between this pair of Tx and Rx. The bending angle α, elevation angle β and transmission T along a ray path can be expressed in terms of the impact parameter a. Thus, a relation between T and β can be obtained in the form of a curve in the βT plane, as presented in Eq. (4).

2.2. Differential Transmission over a Channel Pair

Along a ray path from Tx to Rx, in addition to the absorption by the target species, there are other loss mechanisms, including absorption by foreign species, defocusing, Rayleigh scattering, aerosol extinction, cloud extinction, turbulence-induced scintillation, Doppler shift caused by line-of-sight winds, and solar radiation scattered by clouds [19]. To minimize these effects, differential transmission will be used to retrieve the profile of the target species [4, 5]. It requires proper selection of an adjacent pair of channels, with one channel assigned at the center of an absorption line of the target species and the other reference channel which is off the absorption line of any trace species.

The measured transmissions in the absorption channel (T^{mea}) and the reference channel (T^{mer}) can be decomposed as

$$T^{\text{mea}}(\beta) = T_t^a(\beta) + T_f^a(\beta) + T_a^a(\beta) \tag{5}$$

$$T^{\text{mer}}(\beta) = T_t^r(\beta) + T_f^r(\beta) + T_a^r(\beta) \tag{6}$$

where $T_t^a(\beta)$, $T_f^a(\beta)$ and $T_a^a(\beta)$ are the transmissions attributed to the target species, its major foreign species and other atmospheric effects, respectively, in the absorption channel; $T_t^r(\beta)$, $T_f^r(\beta)$ and $T_a^r(\beta)$ are their counterparts in the reference channel. These two channels are preferred to be sufficiently close so that the atmospheric effects on both channels are close ($< 0.1\%$ [4, 19]), namely, $T_a^a(\beta) \simeq T_a^r(\beta)$. By subtracting Eq. (6) from Eq. (5), we obtain the differential transmission

$$\Delta T^{\text{me}}(\beta) = T^{\text{mea}}(\beta) - T^{\text{mer}}(\beta) \simeq \Delta T_t(\beta) + \Delta T_f(\beta) \tag{7}$$

where $\Delta T_\alpha(\beta) = T_\alpha^a(\beta) - T_\alpha^r(\beta)$, with $\alpha = t, f$. Except for cloud extinction, the other atmospheric effects account for 0.1% or less in a typical spaced-based LIO technique [19], which is assumed valid in the LGIO technique.

The volume mixing ratio (VMR) of the target species, $\chi^{\text{re}}(h)$ (in ppmv), can be retrieved by minimizing the difference between the differential transmission of the target species ($\Delta T_t(\beta)$) and the modeled differential transmission of it ($\Delta T_t^{\text{mo}}(\beta)$) as

$$\chi^{\text{re}}(h) = \arg\min_{\chi(h)} \left\{ \sum_{j=1}^{J} [\Delta T_t(\beta_j) - \Delta T_t^{\text{mo}}(\beta_j)]^2 \right\} \tag{8}$$

where J is the number of measurement data, $\Delta T_t^{\text{mo}}(\beta_j) = T_t^{\text{moa}}(\beta_j) - T_t^{\text{mor}}(\beta_j)$ the modeled differential transmission at an elevation angle β_j, and the superscript re indicates the retrieved VMR of the target species.

The modeled transmissions in the absorption and reference channels of the target species, T_t^{moa} and T_t^{mor}, are derived from the modeled absorption coefficients of the target species, k_t^{moa} (1/m) and k_t^{mor} (1/m), as $k_t^{\text{moa}} = \kappa_t^{\text{moa}} \rho_t^{\text{mo}}$ and $k_t^{\text{mor}} = \kappa_t^{\text{mor}} \rho_t^{\text{mo}}$, where κ_t^{moa} (m^2/kg) and κ_t^{mor} (m^2/kg) are the modeled mass absorption coefficients of the target species, and ρ_t^{mo} (kg/m^3) is the modeled mass density of the target species.

The absorption coefficients are functions of height, which can be expressed in terms of the modeled VMR profile (χ^{mo}) as [4]

$$\begin{aligned} k_t^{\text{moa}}(h) &= 10^{-6} \times \frac{m_g \kappa_t^{\text{moa}}(h) P(h)}{R_d T_0(h)} \chi_t^{\text{mo}}(h) \\ k_t^{\text{mor}}(h) &= 10^{-6} \times \frac{m_g \kappa_t^{\text{mor}}(h) P(h)}{R_d T_0(h)} \chi_t^{\text{mo}}(h) \end{aligned} \tag{9}$$

where $\rho = 10^{-6} \times \frac{m_g P}{R_d T_0} \chi_t$ (kg/m^3); $R_d = 8.3145$ J/K/mole is the universal molar gas constant, and m_g (kg/mole) is the molecular weight of the target species. The modeled mass absorption coefficients in the absorption channel and reference channel are $\kappa_t^{\rm moa}$ (m^2/kg) and $\kappa_t^{\rm mor}$ (m^2/kg), respectively, which are calculated by using the line parameters in the HITRAN database [21], given the profiles of pressure P (Pa), temperature T_0 (K) and VMR of air, χ_t (ppm).

Note that the data $\Delta T_t(\beta_j)$ to be substituted into Eq. (8) for the retrieval of the VMR profile is derived by subtracting $\Delta T_f(\beta_j)$ from the measured data of $\Delta T^{\rm me}(\beta_j)$. For a given target species, $\Delta T_f(\beta_j)$ can be estimated by using the line parameters in the HITRAN database [21], under given profiles of pressure, temperature and air composition, with the VMR profiles of GHGs derived with the FASCODE model [18].

Since each target species behaves as a foreign species to the other target species, the VMRs of all the foreign species will be updated alternatively, as will be described in more details about the retrieval flow-chart shown in Figure 5. Let the estimated value of $\Delta T_f(\beta_j)$ be $\Delta T_f^{\rm es}(\beta_j)$, then $\Delta T_t(\beta_j)$ will be estimated from Eq. (7) as

$$\Delta T_t^{\rm es}(\beta_j) = \Delta T^{\rm me}(\beta_j) - \Delta T_f^{\rm es}(\beta_j) \tag{10}$$

which will be substituted into Eq. (8) for retrieving the target VMR profile.

2.3. Selection of Target GHG Species

In this work, the channels will be selected from those listed in Table 1 [4, 5], where $\nu_{\rm abs}$ and $\nu_{\rm ref}$ are the wavenumbers (1/cm) in the absorption and the reference channels, respectively. For each of the absorption channels, a reference channel is selected within a relative spectral separation of $\pm 1\%$ or $\pm 0.5\%$ if possible, based on the criterion that the absorption in the reference channel is mainly attributed to the atmospheric effects [2].

In Table 1, 12 channel pairs were selected for the retrieval of CH_4, CO_2, H_2O and O_3 [4]. Four absorption channels were selected to retrieve the H_2O profile. The H_2O-1 channel is most sensitive to H_2O absorption, and was used at heights of 13 to 40 km, under all atmospheric conditions. The H_2O-4 channel is least sensitive to H_2O absorption, and was used at heights below 7 km, under wet tropical condition. The H_2O-2 and H_2O-3 channels were used to cover the heights of 8–25 km and 5–10 km, respectively. Since the absorption by H_2O increases significantly in the lower troposphere, we choose the least sensitive channel, H_2O-4 channel, as the H_2O absorption channel in this work.

Table 1. Absorption and reference channels of gas species considered in this work [4].

Order	Species	$\nu_{\rm abs}$ (1/cm)	$\nu_{\rm ref}$ (1/cm)
1	N_2O	4710.340810	4731.03
2	CH_4	4344.163500	4322.93
3	$^{13}CO_2$	4723.414953	4731.03
4	$C^{18}OO$	4767.041369	4770.15
5	H_2O-1	4204.840290	4227.07
5	H_2O-2	4775.802970	4770.15
5	H_2O-3	4747.054840	4731.03
5	H_2O-4	4733.045010	4731.03
6	$^{12}CO_2$	4771.621441	4770.15
7	HDO	4237.016320	4227.07
8	$H_2^{18}O$	4090.871800	4098.56
9	CO	4248.317600	4227.07
10	O_3	4029.109610	4037.21

Table 2. Transmissions of target and major foreign species with LGIO technique.

Species	T_f^a (dB), major	T_f^r (dB), major	T_t^a (dB)	T_t^r (dB)	$\lvert\Delta T_f\rvert/\lvert\Delta T_t\rvert$
N_2O	H_2O:−0.32, CO_2:−0.019	CO_2:−0.15, H_2O:−0.04	−5.7	−0.025	0.06
CH_4	H_2O:−0.31, N_2O:−0.0076	H_2O:−0.02, N_2O:−0.0045	−8.2	-1.1×10^{-3}	0.03
$^{13}CO_2$	H_2O:−0.6, N_2O:−0.25	CO_2:−0.16, H_2O:−0.04	−0.1	-9×10^{-4}	5.6
$C^{18}OO$	H_2O:−1, CO_2:−0.7	CO_2:−0.55, H_2O:−0.028	−0.03	−0.001	33.3
H_2O	CO_2:−0.5, N_2O:−0.147	CO_2:−0.16, N_2O:−0.025	−23	−0.04	0.015
$^{12}CO_2$	H_2O:−2, $C^{18}OO$: −0.0016	H_2O:−0.028	−27	−0.55	0.075
HDO	H_2O:−2.5, CO_2:−0.02	CO:−0.2, H_2O:−0.15	−0.008	-7×10^{-5}	293
$H_2^{18}O$	H_2O:−52, N_2O:−0.0011	H_2O:−0.126	−0.17	-6×10^{-5}	742
CO	H_2O:−4.43	H_2O:−0.1533	−5.75	−0.21	0.77
O_3	H_2O:−374	H_2O:−4.4	−4.96	-9×10^{-4}	75.4

T_f^a: transmission attributed to major foreign species in absorption channel of target species,
T_f^r: transmission attributed to major foreign species in reference channel of target species,
T_t^a: transmission attributed to target species in absorption channel of target species,
T_t^r: transmission attributed to target species in reference channel of target species,
$|\Delta T_f|/|\Delta T_t|$: ratio of differential transmissions attributed to foreign species and target species, respectively.

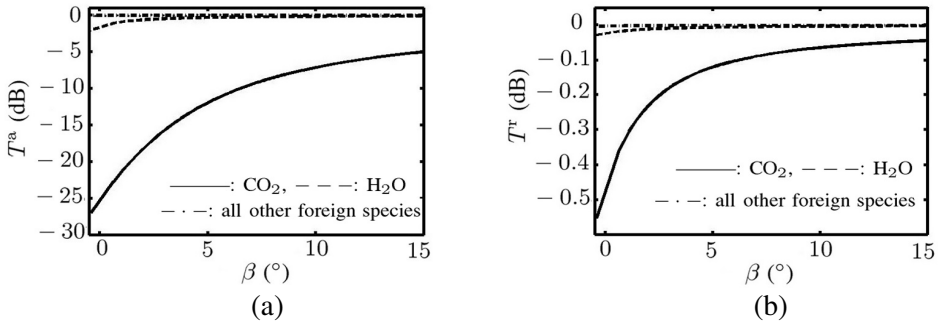

Figure 2. Transmission in (a) absorption channel and (b) reference channel selected for CO_2.

In this work, the four species, H_2O, CO_2, N_2O and CH_4, will be retrieved for their VMR profiles via Eq. (8). The channel pairs are selected such that the contribution by foreign species is negligibly small, $|\Delta T_f| \ll |\Delta T_t|$. However, as a ray path traverses near ground, the width of H_2O absorption lines are increased [21], and some of the H_2O absorption lines in the SWIR band may shift too close to the absorption or reference channels selected for other species. As the mass density of H_2O increases exponentially near ground, the VMR retrieval of other species may be affected even more serious. This issue will be analyzed later, as summarized in Table 2.

Figure 2 shows the transmission attributed to different species in the absorption and reference channels, respectively, selected for CO_2, based on the US standard atmosphere in the FASCODE model. As the elevation angle increases from $-0.4°$ to $15°$, T_t^a increases from -27 to -5 dB and T_t^r increases from -0.55 to -0.05 dB. It is observed that changing the VMR profile leads to insignificant change in the differential transmission as $\beta > 15°$. Hence, the maximum elevation angle is set to $15°$. For the retrieval of CO_2 profile, H_2O is the major foreign species, with its contribution increasing from -2 to -0.1 dB in the CO_2 absorption channel, and from -0.028 to -0.0019 dB in the CO_2 reference channel. The other foreign species have negligible contribution in these two channels. Thus, the condition $|\Delta T_f| \leq 0.1|\Delta T_t|$ holds in retrieving the CO_2 profile.

Figure 3 shows the transmission attributed to different species in the absorption and reference channels, respectively, selected for CO. As the elevation angle increase from $-0.4°$ to $15°$, T_t^a increases

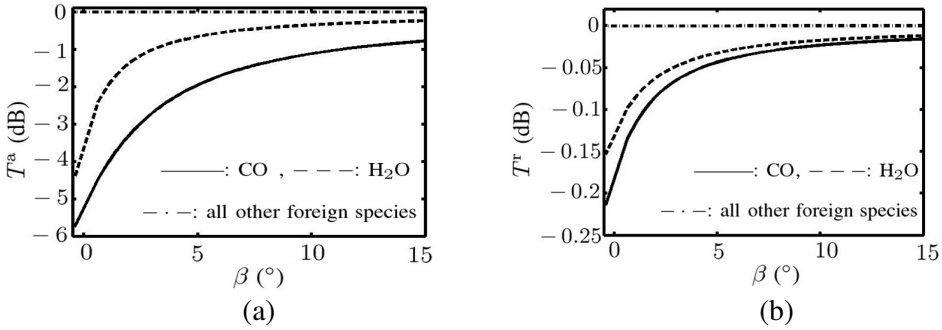

Figure 3. Transmission in (a) absorption channel and (b) reference channel selected for CO.

from −5.75 to −0.9 dB, and T_t^r increases from −0.21 to −0.02 dB. H_2O is the major foreign species to CO, with its contribution increasing from −4.43 to −0.2 dB in the CO absorption channel, and from −0.15 to −0.019 dB in the CO reference channel. The other foreign species contribute a differential transmission smaller than 0.001 dB and can be neglected. Since $|\Delta T_f| \simeq 0.7|\Delta T_t|$, the foreign species will compromise the retrieval of CO profile. Hence, the LGIO technique with the same channels as selected for its space-based counterpart will not work in retrieving the CO profile.

Table 2 lists the transmissions of major GHGs and their major foreign species in the absorption and the reference channels, respectively. These data are calculated at the minimal elevation angle of $\beta = -0.4°$, with the spectral-line data from the HITRAN molecular absorption database, under the standard atmosphere of the FASCODE model. The LEO satellite is assumed to have an inclination of about 80° and an orbit height of 600 km, and the pulse repetition frequency of the IR laser is 10 Hz, the same as that in the ACCURATE mission [2].

It is observed that the influence of H_2O on isotopes $^{13}CO_2$, $C^{18}OO$, HDO and $H_2^{18}OO$ as well as CO and O_3 are quite large, as compared to the other species, N_2O, CH_4, H_2O and $^{12}CO_2$. Hence, the last four species are chosen as the target species to apply the proposed LGIO technique. The channels selected for retrieving the four major species have different sensitivities to the absorption of foreign species. The species with least sensitivity to other species will be retrieved first, followed by the species with the second least sensitivity, and so on. Based on this criterion, H_2O is retrieved first because it has the smallest ratio of $|\Delta T_f|/|\Delta T_t|$, CH_4 is retrieved the next, followed by N_2O and CO_2.

2.4. Link Budget of an LGIO Mission

Table 3 lists the parameters used to determine the link budget of an LGIO mission. The laser pulse power is $P_t = 10$ W, which is available in wireless power transmission [22], and the laser beam divergence is $\alpha_t = 3$ mrad at full angle. The range of elevation angle is $-0.4° \le \beta \le 15°$, $R_e = 6,400$ km and $h_{\mathrm{LEO}} = 600$ km. The reception telescope is of the Cassegrain type, with diameter $d_1 = 0.36$ m [23, 24]. The error on differential transmission due to reflector distortion is negligible. Typical transmissions $T^a(\beta_{\min})$ in the absorption channel, at the minimal elevation angle $\beta_{\min}$, for H_2O, CH_4, N_2O and CO_2 are −23, −9, −6 and −27 dB, respectively, under the US standard atmosphere.

Figure 4 shows the factors considered in determining the link budget of an LGIO mission. Typical transmission attributed to atmospheric effects and foreign absorption are $T_{\mathrm{atm}} = -0.5$ dB and $T_f = -2$ dB, respectively. The reception loss L_{rec} is the ratio of pulse durations at Tx and Rx, which is 1.5 ms/2 ms = 0.75. The total optical loss, which is assumed to be $L_o = 35\%$, is the attenuation from the front optics to the detector, including central obscuration. The propagation loss is calculated as [2]

$$L_p = \frac{2\pi \int_0^{d_1/2} e^{-(\rho')^2/(w_1^2/2)} \rho' d\rho'}{2\pi \int_0^{w_1} e^{-(\rho')^2/(w_1^2/2)} \rho' d\rho'} = \frac{1 - e^{-d_1^2/(2w_1^2)}}{1 - e^{-2w_1^2/w_1^2}} \simeq \frac{d_1^2/(2w_1^2)}{1 - e^{-2}} \simeq 2\frac{A_1}{w_1^2 \pi}$$

where $w_1 = R\alpha_t/2$ is the Gaussian-beam radius (down to e^{-2} of the maximum intensity) at the reception site, $A_1 = \pi d_1^2/4$ is the receiver aperture with diameter d_1. The signal-to-noise ratio is

Table 3. Link budget of an LGIO mission.

parameter	budget (in dB)
P_t	$10\,\mathrm{dB_W}$
$L_p(\beta)$	-104.5 to $-99.6\,\mathrm{dB}$
L_{rec}	$-1.25\,\mathrm{dB}$ (1.5 ms/2 ms)
L_o	$-1.85\,\mathrm{dB}$ (65%)
$P_{r,0}(\beta)$	-77.6 to $-72.7\,\mathrm{dB_W}$
noise equivalent power (NEP) of IR detector system within 2 ms	$-121.4\,\mathrm{dB_W}$
$\mathrm{SNR}_0(\beta)$ (without attenuation due to atmosphere and GHGs)	43.8 to 48.7 dB
$T^a(\beta)$ of H_2O	$-23\,\mathrm{dB}$ to $-1.7\,\mathrm{dB}$
$T^a(\beta)$ of CH_4	$-8.2\,\mathrm{dB}$ to $-1.2\,\mathrm{dB}$
$T^a(\beta)$ of N_2O	$-5.7\,\mathrm{dB}$ to $-1\,\mathrm{dB}$
$T^a(\beta)$ of CO_2	$-27\,\mathrm{dB}$ to $-5\,\mathrm{dB}$
$\lvert T_{\mathrm{atm}}\rvert$	$\leq 0.5\,\mathrm{dB}$
$\lvert T_f\rvert$	$\leq 2\,\mathrm{dB}$
achieved $\mathrm{SNR}(\beta)$	16.8 to 47 dB

All parameters except P_t are the same as in [2].
These values are derived under the US standard atmosphere.

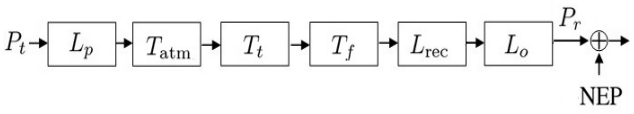

Figure 4. Factors considered in determining the link budget of an LGIO mission.

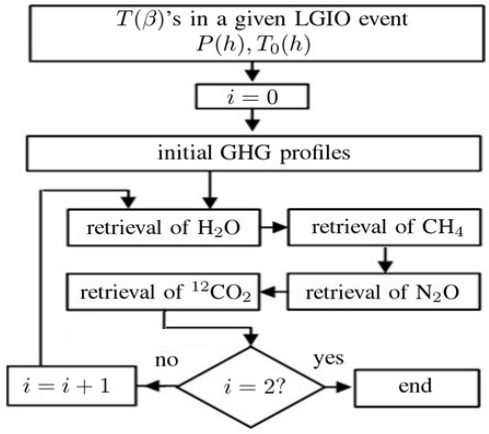

Figure 5. Flow-chart for retrieving VMR profiles of GHGs.

$\mathrm{SNR}_0 = P_{r0}/\mathrm{NEP}$, where P_{r0} is the received power without atmospheric effects or gas absorption, and NEP is the noise equivalent power, which is assumed to be independent of the signal intensity.

3. HS-EC ALGORITHM FOR RETRIEVING GHG PROFILES

Figure 5 shows the flowchart for retrieving the VMR profiles of GHGs, given the estimated profiles of pressure, temperature and transmission data. The species less sensitive to foreign species is retrieved before that more sensitive to foreign species. Thus, the H_2O profile is retrieved first, followed by those of CH_4, N_2O and CO_2. The most updated GHG profiles will be used to determine the transmissions in the channel pair of a target species, to be used as $\Delta T_f^{\mathrm{es}}(\beta_j)$ in Eq. (10). Then, the differential transmission of the target species, $\Delta T_t^{\mathrm{es}}(\beta_j)$, will be updated with (10). Note that the refractivity profile is slightly

affected by the water-vapor pressure, and can be updated by using Eq. (1).

Next, a harmony search (HS) algorithm [15, 25] is applied to find the optimal VMR profile defined in Eq. (8). A harmony vector is defined as $\bar{\chi} = [\chi_1, \chi_2, \ldots, \chi_M]$, where χ_m is the VMR value at altitude h_m and M is the number of altitude levels. To begin with, a harmony memory (HM) is initialized, by random tuning, as

$$\mathrm{HM} = \begin{bmatrix} \chi_{1,1} & \chi_{2,1} & \cdots & \chi_{\mathrm{HMS},1} \\ \chi_{1,2} & \chi_{2,2} & \cdots & \chi_{\mathrm{HMS},2} \\ \vdots & \vdots & \ddots & \vdots \\ \chi_{1,M} & \chi_{2,M} & \cdots & \chi_{\mathrm{HMS},M} \end{bmatrix}$$

where M and HMS denote the number of musicians and the size of harmony memory, respectively; $\chi_{n,m}$ is the nth harmony of the mth musician. Typically, the HM is arranged such that a column vector with smaller object function is placed before that with larger one.

Ensemble consideration (EC) is implemented by generating candidate column vectors for HM that resemble a reference VMR profile, $\bar{\chi}^{\mathrm{EC}}$. A new column vector $\bar{\chi}^{\mathrm{new}}$ can be generated as

$$\chi_m^{\mathrm{new}} = \chi_{m-1}^{\mathrm{new}} \frac{\chi_m^{\mathrm{EC}}}{\chi_{m-1}^{\mathrm{EC}}} + c_1 \times U(-1,1) \times \mathrm{FW}_m \tag{11}$$

with $2 \le m \le M$, where $U(\alpha, \beta)$ is a uniform distribution over an interval (α, β); $\mathrm{FW}_m = \chi_m^U - \chi_m^L$ is the fret width of the mth musician [15]; χ_m^U and χ_m^L are the upper and lower bounds, respectively, of χ_m. Alternatively, $\bar{\chi}^{\mathrm{new}}$ can be generated as

$$\chi_m^{\mathrm{new}} = \chi_{m-1}^{\mathrm{new}} \frac{\chi_{p,m}}{\chi_{p,m-1}} \tag{12}$$

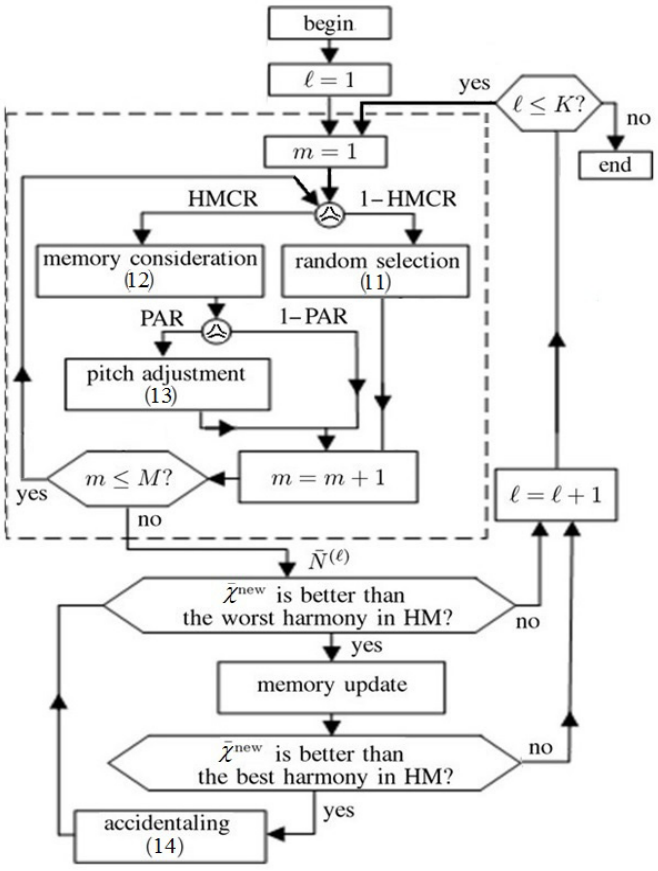

Figure 6. Flow-chart of HS-EC algorithm for retrieving VMR profiles of GHGs.

with $p = \lfloor U^2(0,1) \times \mathrm{HMS} \rfloor + 1$, where $\lfloor r \rfloor$ is the integer part of a positive real number r. In this work, $\bar{\chi}^{\mathrm{EC}}$ is derived from the standard atmosphere in the FASCODE model [18]. The VMR value measured on the ground can be used as χ_1^{EC}. A candidate column vector will be generated by using (11) with a probability of 1 − HMCR and by using Eq. (12) with a probability of HMCR.

An adjust-pitch process is implemented, with probability of PAR, to update $\bar{\chi}^{\mathrm{new}}$ as

$$\chi_m^{\mathrm{new}} = \chi_{m-1}^{\mathrm{new}} + c_1 \times U(-1,1) \times \mathrm{FW}_m \tag{13}$$

If $\bar{\chi}^{\mathrm{new}}$ violates any constraint, for example, exceeds the upper or lower bound, it will be abandoned. If $\bar{\chi}^{\mathrm{new}}$ is better than the worst harmony in HM in terms of object function, the latter will be replaced by $\bar{\chi}^{\mathrm{new}}$. If $\bar{\chi}^{\mathrm{new}}$ turns out to be better than all column vectors in the HM, an accidentaling process will be applied to update the former as

$$\chi_m^{\mathrm{new}} = \chi_m^{\mathrm{new}} + c_2 \times U(-1,1) \times \mathrm{FW}_m \tag{14}$$

where c_2 is a weighting coefficient used to fine-tune the best candidate. The weighting coefficients c_1 and c_2 decrease linearly from $c_{1,0}$, $c_{2,0}$, respectively, to zero as the iteration process proceeds. The idea is to encourage exploration in the early stage and to encourage convergence to an optimum solution near the end of the iteration process [26]. Figure 6 shows a flow-chart of the HS-EC algorithm for retrieving the VMR profiles of GHGs, where the maximum iteration number is set to $K = 20,000$.

4. KEY FACTORS TO RETRIEVE ACCURATE VMR PROFILES

4.1. Sensitivity of Target VMR Profiles on Differential Transmission

By substituting (7) into Eq. (10), we have

$$\Delta T_t^{\mathrm{es}} - \Delta T_t \simeq \Delta T_f - \Delta T_f^{\mathrm{es}} \tag{15}$$

which implies that the estimation error of the target differential transmission, $\Delta T_t^{\mathrm{es}} - \Delta T_t$, is roughly equal to that of the foreign species, $\Delta T_f - \Delta T_f^{\mathrm{es}}$. A variation of VMR profile leads to a variation of the target differential transmission. It will be useful to analyze the effects of VMR variation of target species and the error $|\Delta T_f - \Delta T_f^{\mathrm{es}}|$ caused by foreign species, respectively, on the resolution of the target differential transmission.

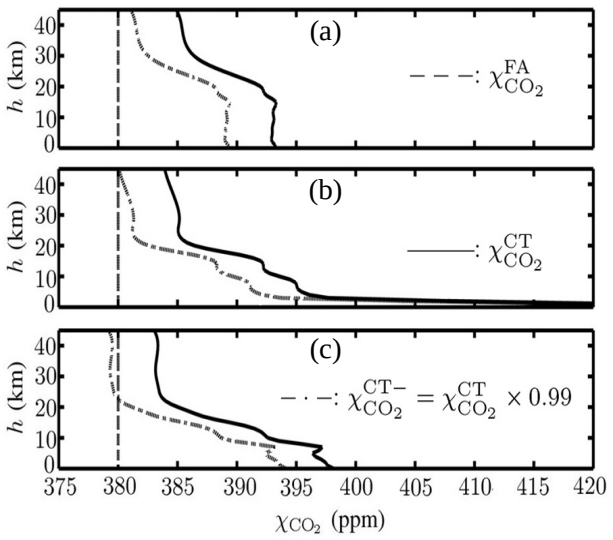

Figure 7. VMR Profiles of CO_2 at (a) (1.1°N, 86°W) (Trop), (b) (39.7°N, 114°W) (NHM) and (c) (67.5°N, 7.3°E) (NHP); UTC 00:00 2012/12/1.

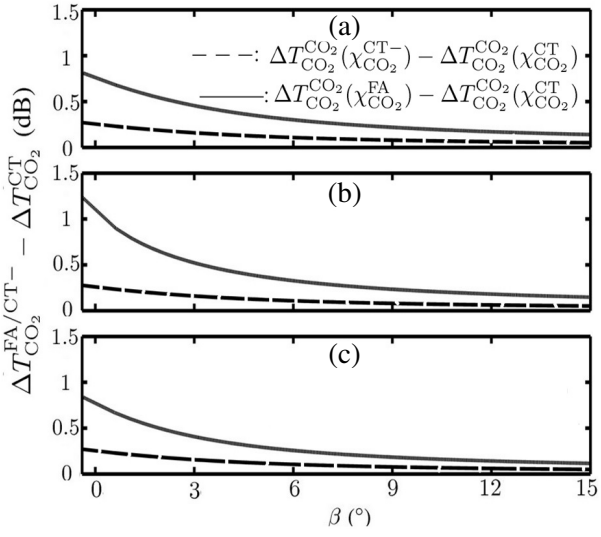

Figure 8. Difference of differential transmissions with different VMR profiles of CO_2 at (a) (1.1°N, 86°W) (Trop), (b) (39.7°N, 114°W) (NHM) and (c) (67.5°N, 7.3°E) (NHP); UTC 00:00 2012/12/1.

Figure 7 shows the VMR profiles CO_2 at three locations, (1.1°N, 86°W), (39.7°N, 114°W) and (67.5°N, 7.3°E), representing tropical (Trop), mid-latitude winter (NHM) and subarctic winter (NHP) atmospheres, respectively; at UTC 00:00 2012/12/1, which is the latest time mark of data available from the CT model. At each location, the CT model and FASCODE model are applied to obtain $\chi^{\mathrm{CT}}_{\mathrm{CO_2}}$ and $\chi^{\mathrm{FA}}_{\mathrm{CO_2}}$, respectively, and $\chi^{\mathrm{CT-}}_{\mathrm{CO_2}}$ is derived by multiplying $\chi^{\mathrm{CT}}_{\mathrm{CO_2}}$ with 0.99. The VMR profile derived with the FASCODE model is a constant of 380 ppm from ground to 45 km at height, which is independent of site on the globe. On the other hand, the VMR profile $\chi^{\mathrm{CT}}_{\mathrm{CO_2}}$ generally decreases with height and is site dependent. The VMR profile $\chi^{\mathrm{CT-}}_{\mathrm{CO_2}}$ will be used to calculate the variation of transmission profile when the VMR profile of CO_2 is reduced by 1%.

Figure 8 shows the difference of differential transmission profiles between two VMR profiles of $^{12}CO_2$ as shown in Figure 7, where the superscript CO_2 in $\Delta T^{\mathrm{CO_2}}_{\mathrm{CO_2}}$ means the differential transmission is measured in the channel pair selected for CO_2. Since $\chi^{\mathrm{FA}}_{\mathrm{CO_2}}$ and $\chi^{\mathrm{CT-}}_{\mathrm{CO_2}}$ are smaller than $\chi^{\mathrm{CT}}_{\mathrm{CO_2}}$, $\Delta T^{\mathrm{CO_2}}_{\mathrm{CO_2}}(\chi^{\mathrm{FA}}_{\mathrm{CO_2}})$ and $\Delta T^{\mathrm{CO_2}}_{\mathrm{CO_2}}(\chi^{\mathrm{CT-}}_{\mathrm{CO_2}})$ are larger than $\Delta T^{\mathrm{CO_2}}_{\mathrm{CO_2}}(\chi^{\mathrm{CT}}_{\mathrm{CO_2}})$. As the elevation angle increases from −0.4° to 15°, $\Delta T^{\mathrm{CO_2}}_{\mathrm{CO_2}}(\chi^{\mathrm{FA}}_{\mathrm{CO_2}}) - \Delta T^{\mathrm{CO_2}}_{\mathrm{CO_2}}(\chi^{\mathrm{CT}}_{\mathrm{CO_2}})$ decreases from 0.8 to 0.15 dB in the Trop and NHP atmospheres, and decreases from 1.2 to 0.17 dB in the NHM atmosphere; $\Delta T^{\mathrm{CO_2}}_{\mathrm{CO_2}}(\chi^{\mathrm{CT-}}_{\mathrm{CO_2}}) - \Delta T^{\mathrm{CO_2}}_{\mathrm{CO_2}}(\chi^{\mathrm{CT}}_{\mathrm{CO_2}})$ decreases from 0.27 to 0.045 dB in all three atmosphere models. As shown in Figure 7, the difference between $\chi^{\mathrm{CT}}_{\mathrm{CO_2}}$ and $\chi^{\mathrm{FA}}_{\mathrm{CO_2}}$ becomes larger at lower altitudes. At lower elevation angles, a ray path will traverse the lower atmosphere over a longer distance, which explains such larger difference of differential transmission.

For the system to be sensitive enough to detect 1% difference of VMR between $\chi^{\mathrm{CT-}}_{\mathrm{CO_2}}$ and $\chi^{\mathrm{CT}}_{\mathrm{CO_2}}$, as shown in Figure 7, the receiver is required to be sensitive enough to a resolution of differential transmission, $\delta T_{\mathrm{CO_2}} = \Delta T^{\mathrm{CO_2}}_{\mathrm{CO_2}}(\chi^{\mathrm{CT-}}_{\mathrm{CO_2}}) - \Delta T^{\mathrm{CO_2}}_{\mathrm{CO_2}}(\chi^{\mathrm{CT}}_{\mathrm{CO_2}})$. If the receiver power level is P_r, the corresponding receiver-power sensitivity will be $\delta P_r = P_r(10^{\delta T_{\mathrm{CO_2}}/10} - 1)$.

Figure 9 shows the receiver-power sensitivity, in both the absorption channel and reference channel selected for CO_2, required to detect 1% VMR difference of CO_2. As the elevation angle increases from −0.4° to 15°, δP^a_r increases from −106 to −86 $\mathrm{dB_W}$ and δP^r_r decreases from −78.5 to −82 $\mathrm{dB_W}$. Both are higher than NEP by at least 15 and 39 dB, respectively. Thus, the noise will have negligible effect on the detection of 1% VMR difference of CO_2.

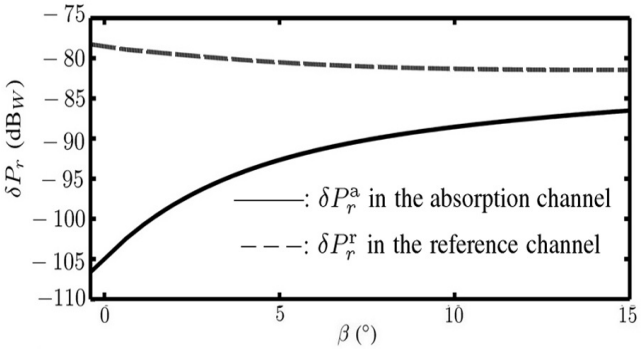

Figure 9. Receiver-power sensitivity required to detect 1% VMR difference of CO_2, NEP = $-121.4\,\mathrm{dB_W}$.

Figure 10(a) shows the VMR profiles of H_2O in the Trop, NHM and NHP atmosphere models, respectively. Figure 10(b) shows the resolution of differential transmission, $\delta T_{\mathrm{H_2O}} = \Delta T^{\mathrm{H_2O}}_{\mathrm{H_2O}}(\chi^{-}_{\mathrm{H_2O}}) - \Delta T^{\mathrm{H_2O}}_{\mathrm{H_2O}}(\chi_{\mathrm{H_2O}})$, where the superscript H_2O in ΔT indicates the channel pair selected for detecting H_2O, and $\chi^{-} = 0.99\chi$. As the elevation angle increases from −0.4° to 15°, $\delta T_{\mathrm{H_2O}}$ with the Trop, NHM and NHP atmospheres decreases from 0.7 to 0.06 dB, from 0.45 to 0.05 dB and from 0.065 to 0.01 dB, respectively. The resolution of differential transmission in the Trop atmosphere is larger than that in

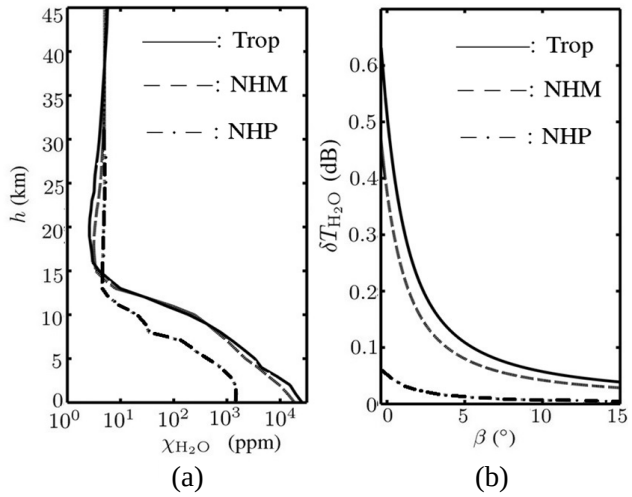

Figure 10. (a) VMR profile $\chi_{\mathrm{H_2O}}$ and (b) resolution profile $\delta T_{\mathrm{H_2O}}$.

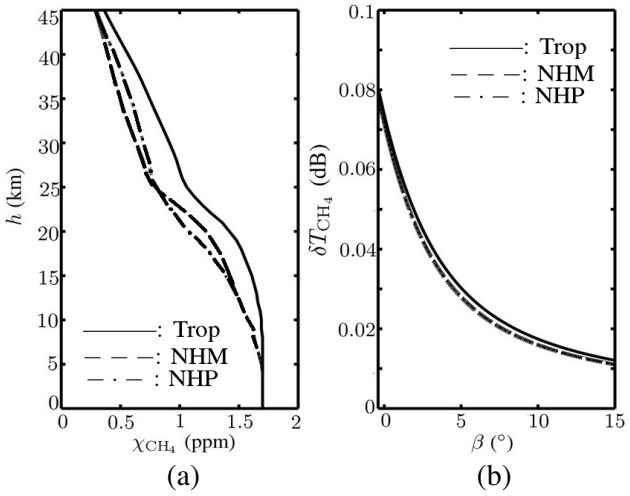

Figure 11. (a) VMR profile $\chi_{\mathrm{CH_4}}$ and (b) resolution profile $\delta T_{\mathrm{CH_4}}$.

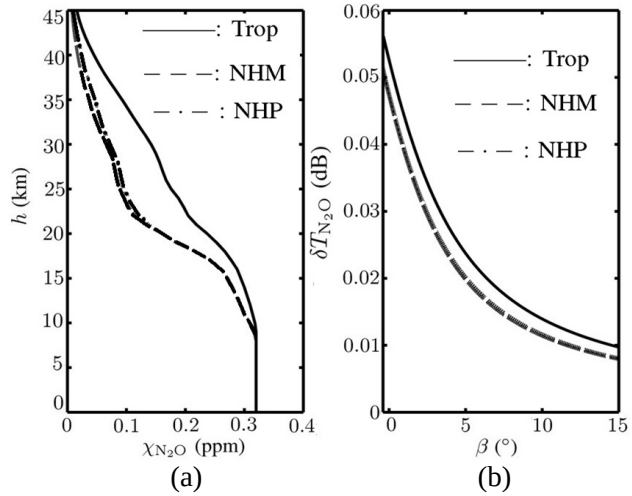

Figure 12. (a) VMR profile $\chi_{\mathrm{N_2O}}$ and (b) resolution profile $\delta T_{\mathrm{N_2O}}$.

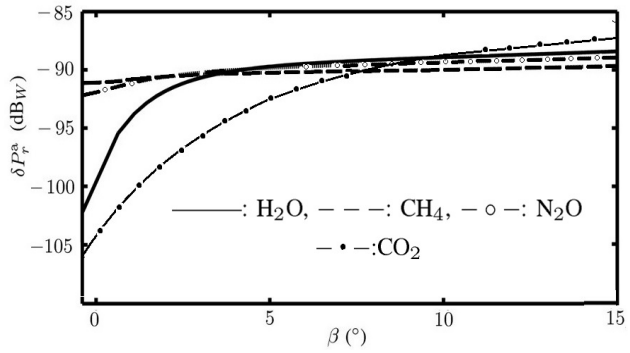

Figure 13. Receiver-power sensitivity required to detect 1% VMR difference of H_2O, CH_4, N_2O and CO_2, respectively; NEP = $-121.4\,\mathrm{dB_W}$.

the NHP atmosphere because the VMR of H_2O is larger in the former.

Figure 11(a) shows the VMR profiles of CH_4 in the Trop, NHM, and NHP atmosphere models, respectively. Figure 11(b) shows the resolution of differential transmission, $\delta T_{\mathrm{CH_4}} = \Delta T^{\mathrm{CH_4}}_{\mathrm{CH_4}}(\chi^-_{\mathrm{CH4}}) - \Delta T^{\mathrm{CH_4}}_{\mathrm{CH_4}}(\chi_{\mathrm{CH_4}})$, where the superscript CH_4 in ΔT indicates the channel pair selected for detecting CH_4, and $\chi^- = 0.99\chi$. As the elevation angle increases from $-0.4°$ to 15°, $\delta T_{\mathrm{CH_4}}$ with the Trop and NHM atmospheres decreases from 0.081 to 0.012 dB and from 0.08 to 0.011 dB, respectively. The profiles of $\delta T_{\mathrm{CH_4}}$ with the NHM and NHP atmospheres almost overlap. Their corresponding VMR profiles of CH_4 are close in magnitude and cross each other at $h = 25\,\mathrm{km}$, thus the optical thicknesses defined in (3) along the same ray path in these two atmosphere models will be close to each other.

Figure 12(a) shows the VMR profiles of N_2O in the Trop, NHM, and NHP atmosphere models, respectively. Figure 12(b) shows the resolution of differential transmission, $\delta T_{\mathrm{N_2O}} = \Delta T^{\mathrm{N_2O}}_{\mathrm{N_2O}}(\chi^-_{\mathrm{N_2O}}) - \Delta T^{\mathrm{N_2O}}_{\mathrm{N_2O}}(\chi_{\mathrm{N_2O}})$, where the superscript N_2O in ΔT indicates the channel pair selected for detecting N_2O,

and $\chi^- = 0.99\chi$. As the elevation angle increases from $-0.4°$ to $15°$, δT_{N_2O} decreases from 0.055 to 0.01 dB in the Trop atmosphere, and from 0.05 to 0.0095 dB in the NHM and NHP atmospheres. The profile of δT_{N_2O} with the NHM and NHP atmospheres almost overlap since the corresponding VMR profiles of N_2O are close to each other.

Figure 13 shows the receiver-power sensitivity required to detect 1% VMR difference of H_2O, CH_4, N_2O and CO_2, respectively. These power sensitivities are higher than the NEP listed in Table 3 by at least 19.4, 30.4, 28.7 and 15 dB, respectively.

4.2. Effects of Foreign Species on Differential Transmission

As listed in Table 2, H_2O is the major foreign species for retrieving the VMR profile of CO_2. Figure 14(a) shows the difference of differential transmission in the channel pair of CO_2, $|\Delta T^{CO_2}_{H_2O}(\chi_{H_2O}) - \Delta T^{CO_2}_{H_2O}(\chi^{es}_{H_2O})|$, when the VMR profile of H_2O is offset by 3%, namely, $\chi^{es}_{H_2O} = 0.97\chi_{H_2O}$. Note that the relative error of VMR estimation in a typical space-based LIO mission is smaller than 3% [4].

As the elevation angle increases from $-0.4°$ to $15°$, the difference $|\Delta T^{CO_2}_{H_2O}(\chi_{H_2O}) - \Delta T^{CO_2}_{H_2O}(\chi^{es}_{H_2O})|$ with the Trop, NHM and NHP atmospheres decreases from 0.2 to 0.01 dB, from 0.14 to 0.0075 dB and from 0.017 to 0.001 dB, respectively. The value with the NHP atmosphere is much smaller than those with the NHM and Trop atmospheres because the former contains much less amount of H_2O than the latter, as shown in Figure 10(a). As compared to δT_{CO_2} shown in Figure 8, $|\Delta T^{CO_2}_{H_2O}(\chi_{H_2O}) - \Delta T^{CO_2}_{H_2O}(\chi^{es}_{H_2O})| < \delta T_{CO_2}$ with these three atmosphere models, which implies that 3% of VMR error in H_2O will not affect the VMR estimation of CO_2.

Similarly, CO_2 is the major foreign species for retrieving the VMR profile of H_2O. Figure 14(b) shows the difference of differential transmission in the channel pair of H_2O, $|\Delta T^{H_2O}_{CO_2}(\chi_{CO_2}) - \Delta T^{H_2O}_{CO_2}(\chi^{es}_{CO_2})|$, when the VMR profile of CO_2 is offset by 3%, namely, $\chi^{es}_{CO_2} = 0.97\chi_{CO_2}$.

As the elevation angle increases from $-0.4°$ to $15°$, $|\Delta T^{H_2O}_{CO_2}(\chi_{CO_2}) - \Delta T^{H_2O}_{CO_2}(\chi^{es}_{CO_2})|$ decreases from 9.4×10^{-3} to 1.3×10^{-3} dB with all three atmosphere models wherein the VMR profiles of CO_2 are slightly different. The value of $|\Delta T^{H_2O}_{CO_2}(\chi_{CO_2}) - \Delta T^{H_2O}_{CO_2}(\chi^{es}_{CO_2})|$ is smaller than δT_{H_2O}, which is shown in Figure 10(b). After three iterations over the flow-chart shown in Figure 5, the effects of foreign species

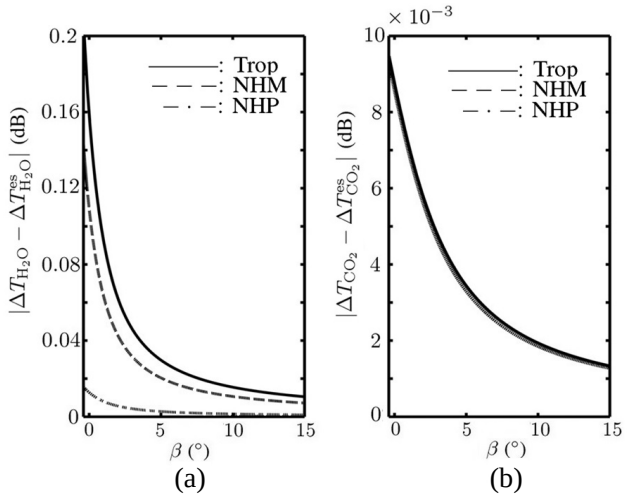

Figure 14. (a) Effect of VMR error in H_2O on the differential transmission of CO_2, $|\Delta T^{CO_2}_{H_2O}(\chi_{H_2O}) - \Delta T^{CO_2}_{H_2O}(\chi^{es}_{H_2O})|$, (b) effect of VMR error in CO_2 on the differential transmission of H_2O, $|\Delta T^{H_2O}_{CO_2}(\chi_{CO_2}) - \Delta T^{H_2O}_{CO_2}(\chi^{es}_{CO_2})|$.

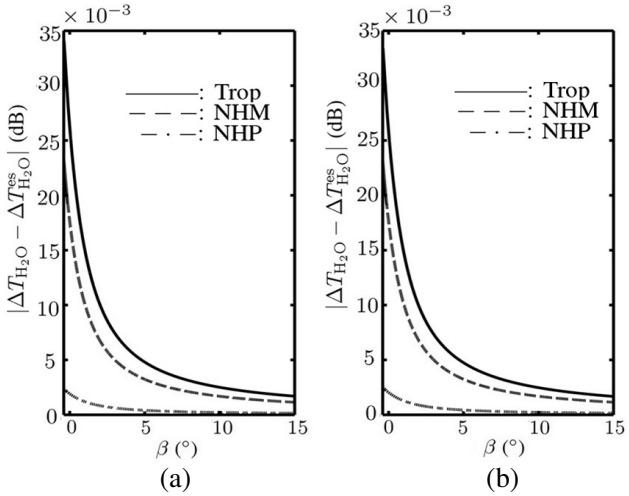

Figure 15. Effect of VMR error in major foreign species (H_2O) on the differential transmission of the target species. (a) $|\Delta T^{CH_4}_{H_2O}(\chi_{H_2O}) - \Delta T^{CH_4}_{H_2O}(\chi^{es}_{H_2O})|$ in CH_4 channel pair, (b) $|\Delta T^{N_2O}_{H_2O}(\chi_{H_2O}) - \Delta T^{N_2O}_{H_2O}(\chi^{es}_{H_2O})|$ in N_2O channel pair.

on the differential transmission of the target species can be significantly reduced.

H_2O is also the major foreign species for retrieving the VMR profiles of CH_4 and N_2O. Figure 15 shows the difference of differential transmission, $|\Delta T_{H_2O}(\chi_{H_2O}) - \Delta T_{H_2O}(\chi^{es}_{H_2O})|$, in the channel pairs of CH_4 and N_2O, respectively, when the VMR profile of H_2O is offset by 3%, namely, $\chi^{es}_{H_2O} = 0.97\chi_{H_2O}$.

As the elevation angle increases from $-0.4°$ to 15°, $|\Delta T^{CH_4}_{H_2O}(\chi_{H_2O}) - \Delta T^{CH_4}_{H_2O}(\chi^{es}_{H_2O})|$ with the Trop, NHM and NHP atmosphere models decreases from 0.034 to 0.0016 dB, from 0.023 to 0.0011 dB and from 0.0024 to 0.00015 dB, respectively. Similarly, $|\Delta T^{N_2O}_{H_2O}(\chi_{H_2O}) - \Delta T^{N_2O}_{H_2O}(\chi^{es}_{N_2O})|$ with the Trop, NHM and NHP atmosphere models decreases from 0.033 to 0.0017 dB, from 0.023 to 0.0011 dB and from 0.0025 to 0.0002 dB, respectively.

In summary, for the four major gas species of interest (H_2O, CH_4, N_2O and CO_2), the difference of differential transmission caused by foreign species is smaller than the resolution of the target differential transmission (δT_t). Thus, the proposed LGIO technique is capable of retrieving their VMR profiles with sufficient accuracy.

4.3. Effects of Thermodynamic Profiles

Estimation errors in the thermodynamic profiles of pressure, temperature and water vapor may also affect the VMR profile of a target species. Figure 16 shows the difference of differential transmission profiles in the CO_2 channel-pair, with respect to the variations of thermodynamic profiles, $\Delta T^{CO_2}_{CO_2}(P', T_0, P_w) - \Delta T^{CO_2}_{CO_2}(P, T_0, P_w)$, $\Delta T^{CO_2}_{CO_2}(P, T'_0, P_w) - \Delta T^{CO_2}_{CO_2}(P, T_0, P_w)$ and $\Delta T^{CO_2}_{CO_2}(P, T_0, P'_w) - \Delta T^{CO_2}_{CO_2}(P, T_0, P_w)$, respectively. The pressure, temperature and water-vapor pressure are derived from the US standard atmosphere of the FASCODE model, and $P' = P \times (1 + 0.2\%)$, $T'_0 = T_0 + 0.5$, $P'_w = P_w \times (1 + 10\%)$. The primed variables are chosen by referring to a performance analysis on microwave occultation [3], in which the retrieval errors of pressure, temperature and water-vapor pressure are below 0.2%, 0.5 K and 10%, respectively.

As the elevation angle increases from 0° to 15°, the difference of differential transmission profile decreases from 0.012 dB to 0.002 dB due to pressure error, decreases from 0.024 dB to 0.005 dB due to temperature error, and is below 0.001 dB due to water-vapor pressure error. All these differences of differential transmission are smaller than the resolution of differential transmission, δT_{CO_2}, which is 0.05 dB. Thus, potential errors embedded in pressure, temperature and water-vapor pressure will not affect the estimation of differential transmission of CO_2.

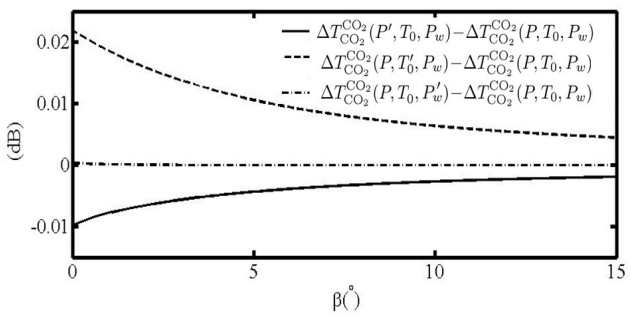

Figure 16. Difference of differential transmission in the channel pair of CO_2, due to variations of thermodynamic profiles.

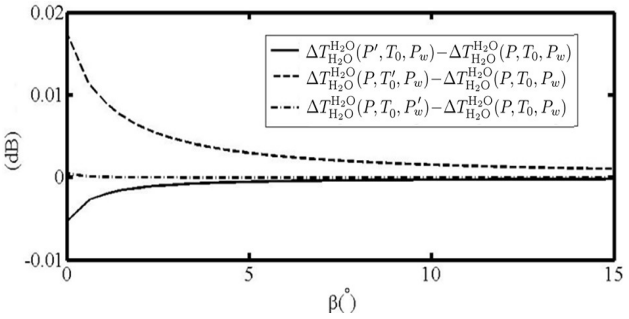

Figure 17. Difference of differential transmission in the channel pair of H_2O, due to variations of thermodynamic profiles.

Similarly, Figure 17 shows the difference of differential transmission profiles in the H_2O channel-pair, with respect to the variations of thermodynamic profiles, $\Delta T^{H_2O}_{H_2O}(P', T_0, P_w) - \Delta T^{H_2O}_{H_2O}(P, T_0, P_w)$, $\Delta T^{H_2O}_{H_2O}(P, T'_0, P_w) - \Delta T^{H_2O}_{H_2O}(P, T_0, P_w)$ and $\Delta T^{H_2O}_{H_2O}(P, T_0, P'_w) - \Delta T^{H_2O}_{H_2O}(P, T_0, P_w)$, respectively. As the elevation angle increases from 0° to 15°, the difference of differential transmission profile decreases from 0.005 dB to 0.001 dB due to pressure error, decreases from 0.017 dB to 0.001 dB due to temperature

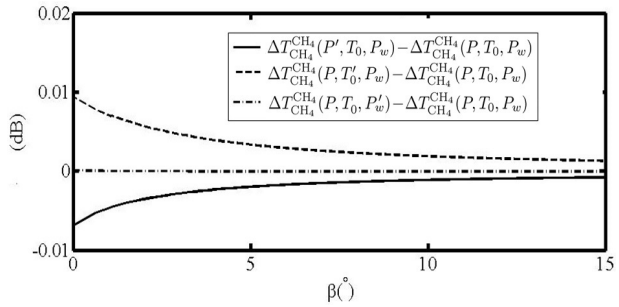

Figure 18. Difference of differential transmission in the channel pair of CH_4, due to variations of thermodynamic profiles.

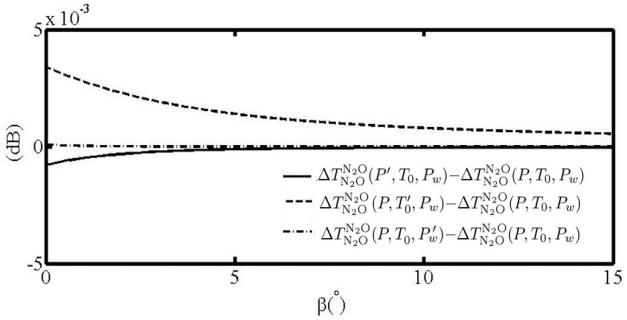

Figure 19. Difference of differential transmission in the channel pair of N_2O, due to variations of thermodynamic profiles.

error, and is below 0.001 dB due to water-vapor pressure error. All these differences of differential transmission are smaller than the resolution of differential transmission, δ_{H_2O}, which is 0.01 dB.

Figure 18 shows the difference of differential transmission profiles in the CH_4 channel-pair, with respect to the variations of thermodynamic profiles, $\Delta T^{CH_4}_{CH_4}(P', T_0, P_w) - \Delta T^{CH_4}_{CH_4}(P, T_0, P_w)$, $\Delta T^{CH_4}_{CH_4}(P, T_0', P_w) - \Delta T^{CH_4}_{CH_4}(P, T_0, P_w)$ and $\Delta T^{CH_4}_{CH_4}(P, T_0, P_w') - \Delta T^{CH_4}_{CH_4}(P, T_0, P_w)$, respectively. As the elevation angle increases from 0° to 15°, the difference of differential transmission profiles decreases from 0.006 dB to 0.001 dB due to pressure error, decreases from 0.0095 dB to 0.0015 dB due to temperature error, and is below 0.001 dB due to water-vapor pressure error. All these differences of differential transmission are smaller than the resolution of differential transmission, δ_{CH_4}, which is 0.01 dB.

Figure 19 shows the difference of differential transmission profiles in the N_2O channel-pair, with respect to the variations of thermodynamic profiles, $\Delta T^{N_2O}_{N_2O}(P', T_0, P_w) - \Delta T^{N_2O}_{N_2O}(P, T_0, P_w)$, $\Delta T^{N_2O}_{N_2O}(P, T_0', P_w) - \Delta T^{N_2O}_{N_2O}(P, T_0, P_w)$ and $\Delta T^{N_2O}_{N_2O}(P, T_0, P_w') - \Delta T^{N_2O}_{N_2O}(P, T_0, P_w)$, respectively. As the elevation angle increases from 0° to 15°, the difference of differential transmission profiles decreases from 0.001 dB to 0.0001 dB due to pressure error, decreases from 0.0035 dB to 0.0005 dB due to temperature error, and is below 0.0003 dB due to water-vapor pressure error. All these differences of differential transmission are smaller than the resolution of differential transmission, δ_{N_2O}, which is 0.01 dB.

4.4. Effects of Defocusing and Rayleigh Scattering

There are other atmospheric effects that may affect the transmission of infrared-laser signals, including wind speed, clouds, aerosols, defocusing and Rayleigh scattering [3]. In this work, it is assumed that the wind speed is zero, and the atmosphere is clear of clouds or aerosols, leaving the effects of defocusing and Rayleigh scattering to be analyzed.

Defocusing or spreading effect is caused by the change in vertical gradient of refractivity, which results in divergence of adjacent, initially parallel ray paths, leading to amplitude variation of [27]

$$A_{ds}(a) = \frac{\sqrt{a}}{\left(r_1 r_2 \sin\theta_0 \sqrt{n_2^2 r_2^2 - a^2}\sqrt{n_1^2 r_1^2 - a^2}\,|d\theta_0/da|_a\right)^{1/2}}$$

The error of differential transmission induced by defocusing or spreading can be defined as $\Delta T_{ds} = 20\log_{10}(A^a_{ds}/A^r_{ds})$, where the superscript a and r refer to the absorption channel and the reference channel, respectively, of the target species.

Figure 20 shows ΔT_{ds} in the CO_2 channel pair, which is below 10^{-6} dB, so are the ΔT_{ds} in the channel pairs of H_2O, CH_4 and N_2O, respectively. Thus, the defocusing effect can be neglected.

The wave intensity attenuated by Rayleigh scattering can be modeled as $I = I_0 \exp\{-\int \sigma_R d\ell\}$, where σ_R (1/m) is the Rayleigh scattering coefficient, and $d\ell$ (m) is a differential length along the ray

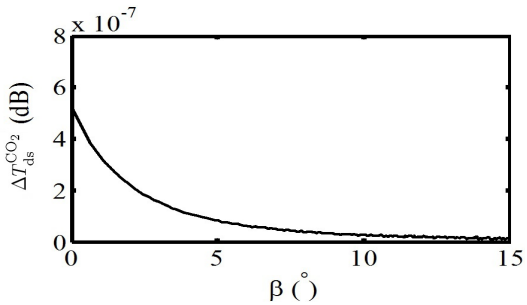

Figure 20. Error of differential transmission, ΔT_{ds}, caused by defocusing or spreading effect in the CO_2 channel pair.

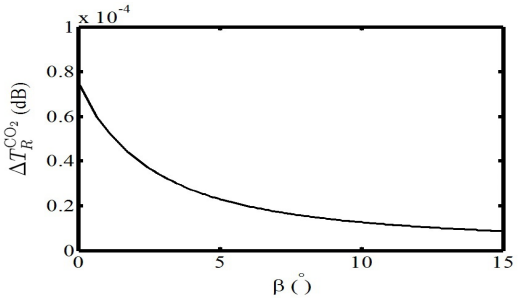

Figure 21. Error of differential transmission in CO_2 channel pair, caused by Rayleigh scattering.

path. The Rayleigh scattering coefficient can be determined as [28]

$$\sigma_R = \frac{32\pi^3(n-1)^2}{3\lambda^4 N_{\text{air}}}$$

where n is the refractive index and N_{air} $(1/\text{m}^3)$ is the number density of air molecules. The error of differential transmission caused by Rayleigh scattering is estimated as

$$\Delta T_R = \left| 10\log_{10}\left\{\int \sigma_R^a d\ell\right\} - 10\log_{10}\left\{\int \sigma_R^r d\ell\right\}\right|$$

Figure 21 shows $\Delta T_R^{\text{CO}_2}$ in the CO_2 channel pair, which is smaller than 10^{-4} dB, so are the ΔT_R in the channel pairs of H_2O, CH_4 and N_2O, respectively. Thus, Rayleigh scattering can be neglected.

5. SIMULATIONS ON RETRIEVING VMR PROFILES

In this section, the proposed LGIO technique is applied by simulations to retrieve the VMR profiles of H_2O, CH_4, N_2O and CO_2. The transmission data at the receiver are simulated with the profiles of CH_4 and N_2O generated with the FASCODE model, and those of CO_2 and H_2O generated with the CT model. The ground-based receivers are placed at the same coordinates as those used in obtaining the results in Figure 7. To implement the HS-EC algorithm, auxiliary profiles are intentionally chosen to be different from those used to simulate the transmission data. In this work, the auxiliary profile of H_2O is generated with the CIRA86aQ_UoG model, and those of the other three species are generated with the US standard atmosphere in the FASCODE model.

The VMR profile will be retrieved from ground to 70 km above ground. The vertical intervals are set to 1 km from the ground level to 20 km at height, 2 km from 22 to 40 km at height, and 5 km from 45 to 70 km at height, making a total of 36 altitude levels. The retrieval accuracy is evaluated by defining a root-mean-square (rms) percentage error as

$$\varepsilon = 100 \times \sqrt{\frac{1}{h_b - h_a}\int_{h_b}^{h_a} \frac{|\chi^{\text{re}}(h) - \chi(h)}{\chi(h)} dh}$$

where $h_a = 0$ and $h_b = 10$ km are chosen to cover the troposphere and the lower stratosphere. The parameters in the HS-EC algorithm are tuned over 100 realizations of simulations in the CO_2 channel pair. It is observed that lower average rms percentage errors of VMR profile can be achieved with the parameters HMS = 100, HMCR = 0.9, PAR = 0.7, $0.04 \le c_{1,0} \le 0.1$ and $0.007 \le c_{2,0} \le 0.02$.

Figure 22 shows the relative error in retrieving the VMR profiles of H_2O and N_2O, respectively. The relative error is smaller than 5% below 5 km of height and is smaller than 10% below 10 km of height. The amount of H_2O is small at high altitudes, hence the absorption by H_2O at high altitudes is significantly small than that at low altitudes. A slight VMR error of H_2O at low altitudes may induce

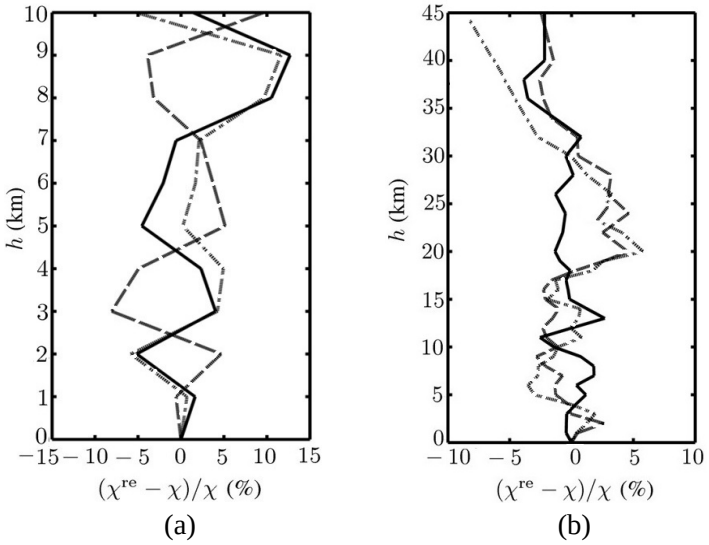

Figure 22. Relative error in retrieved VMR profile of (a) H_2O and (b) CH_4. ———: Trop, − − −: NHM, − · −: NHP.

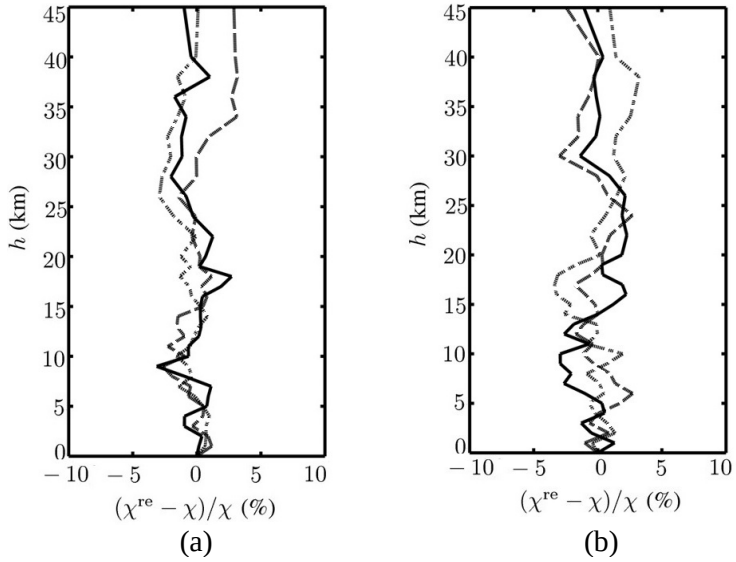

Figure 23. Relative error in retrieved VMR profile of (a) N_2O and (b) CO_2. ———: Trop, −−−:NHM, − · −: NHP.

a large error of absorption at high altitudes in the simulation, leading to large VMR error at high altitudes.

The VMR of H_2O varies over a much wider range than those of the other GHGs of interest. Typical value of χ_{H_2O} varies from 4,000 to 25,000 ppm on the ground at low and mid-latitudes, and is less than 10 ppm above 10 km of height. The VMR error at higher altitudes can be reduced by using additional measurement data from radiosonde, ground-based RO [12], space-based RO [3], space-based LIO [4] or the ECMWF model [17].

The error of differential transmission in the H_2O channel pair, $|\Delta T_f^{H_2O}(\chi^{re}) - \Delta T_f^{H_2O}(\chi)|$, caused by errors in the VMR profiles of foreign species is below 1.5×10^{-3} dB with all three atmosphere models, which is smaller than δT_{H_2O} as shown in Figure 10(b). Similarly, $|\Delta T_f^{CH_4}(\chi^{re}) - \Delta T_f^{CH_4}(\chi)|$ in the CH_4

channel pair is below 2.5×10^{-3} dB with all three atmosphere models, which is smaller than $\delta T_{\mathrm{CH_4}}$ as shown in Figure 11(b), where χ_f and χ_f^{re} are the actual VMR profile and the retrieved VMR profile, respectively, of foreign species.

Figure 23 shows the relative error in retrieving the VMR profiles of N_2O and CO_2, respectively. The relative error from ground to 45 km at height is smaller than 5% for N_2O and smaller than 3% for CO_2. The error of differential transmission in the N_2O channel pair, $|\Delta T_f^{\mathrm{N_2O}}(\chi^{\mathrm{re}}) - \Delta T_f^{\mathrm{N_2O}}(\chi)|$, caused by errors in the VMR profiles of foreign species is below 2.3×10^{-3} dB with all three atmosphere models, which is smaller than $\delta T_{\mathrm{N_2O}}$ as shown in Figure 12(b). Similarly, $|\Delta T_f^{\mathrm{CO_2}}(\chi^{\mathrm{re}}) - \Delta T_f^{\mathrm{CO_2}}(\chi)|$ in the CO_2 channel pair is below 0.012 dB with all three atmosphere models, which is smaller than $\delta T_{\mathrm{CO_2}}$ as shown in Figure 8.

Figure 24 shows the relative error of CO_2 profile at (39.7°N, 114°W), at three instants on June 15, 2012, which implies that the proposed LGIO technique can be applied to monitor the VMR profiles of GHGs around a specific receiver site more frequently. The monthly-averaged VMR profile of CO_2 in June 2005 is derived from the data at latitudes 30°N–40°N in the CT model, to serve as an auxiliary profile in the HS-EC algorithm. It turns out that the VMR error is below 2% from ground to 45 km at height, better than 3% shown in Figure 23(b).

Table 4 lists a general comparison between the conventional space-based LIO and the proposed ground-based LGIO techniques. The LIO technique applies the Abel transform, and the proposed

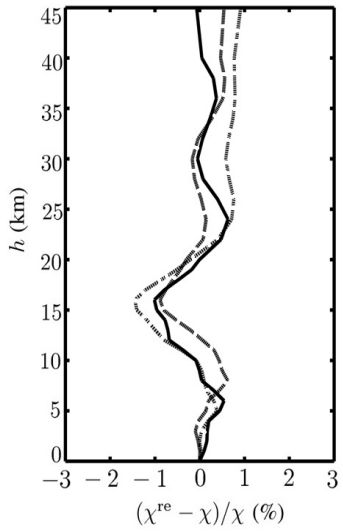

Figure 24. Relative error in retrieved VMR profile of CO_2 in the NHM atmosphere on June 15, 2012. ———: UTC 01:30, − − − UTC 10:30, − · − · −: UTC 19:30.

Table 4. Comparison between conventional space-based LIO technique and proposed ground-based LGIO.

	space-based LEO-LEO infrared laser occultation (LIO)	ground based LEO-ground infrared laser occultation (LGIO)
algorithm	Abel transform	harmony search
accuracy	The root-mean-square (rms) error in retrieved GHG profiles is on the order of 1–3% [4]	The errors in VMR of H_2O, CH_4, N_2O and CO_2 are below 10, 5, 5 and 3%, respectively.
vertical resolution	1 km from 5 km above [4].	1 km from ground level up to 20 km.
simulation time	several seconds	several minutes
required resources	standard PC	standard PC
coverage	global	local

method applies a harmony search algorithm. The rms error in GHG retrieval with LIO is smaller than that with LGIO, partly because the Abel transform applied in LIO renders an explicit solution. In addition, the receivers located near the Earth surface in the ground-based technique may not be able to receive signals coming at negative elevation angles, leading to an ill-posed problem if the Abel transform is to be used. To deal with such a problem, the solution with LGIO is obtained by searching for a transmission profile, as a function of elevation angle, that best fits the measurement profile [13]. In this work, a standard 4-core PC, with i7-3770 CPU (3.4 GHz) and 32 GB RAM, is used. The simulation takes a few seconds for space-based LIO technique and a few minutes for the proposed LGIO technique.

The proposed LGIO technique can complement the LMIO technique for different applications. The latter performs a global GHG monitoring, while the former can be implemented at specific sites of interest to collect data with higher spatial and temporal resolutions. The LGIO technique can also utilize the retrieved GHG profiles at higher altitudes obtained in LMIO missions and focus on retrieving the GHG profiles at lower altitudes with finer resolutions.

6. CONCLUSIONS

A LEO-ground infrared laser occultation (LGIO) technique has been proposed to retrieve the VMR profiles of H_2O and three major GHGs, CO_2, CH_4 and N_2O, by applying a harmony search with ensemble consideration (HS-EC) algorithm. The proposed LGIO technique is capable of retrieving the GHG profiles around a specific receiver site in nearly real time, from ground level up to 45 km at height. The retrieving order of these four species is determined by the effects of major foreign species in the absorption channel of each target species. A link budget and the sensitivity to foreign species have been carefully analyzed to make this LGIO technique more practical. Possible effects of thermodynamic profiles (pressure, temperature and water vapor), atmospheric effects (defocusing and Rayleigh scattering) have also been analyzed. Optimal range of parameters in the HS-EC algorithm suitable for this task are also acquired by simulations.

REFERENCES

1. Kursinski, E. R., G. A. Hajj, W. I. Bertiger, S. S. Leroy, T. K. Meehan, L. J. Romans, J. T. Schofield, D. J. McCleese, W. G. Melbourne, and C. L. Thornton, "Initial results of radio occultation observations of Earth's atmosphere using the Global Positioning System," *Science*, Vol. 271, No. 5252, 1107–1110, 1996.
2. Schweitzer, S., "The ACCURATE concept and the infrared laser occultation technique: Mission design and assessment of retrieval performance," *Sci. Rep.*, No. 34, Wegener Center for Climate and Global Change, Univ. of Graz, Jun. 2010.
3. Schweitzer, S., G. Kirchengast, M. Schwaerz, J. Fritzer, and M. E. Gorbunov, "Thermodynamic state retrieval from microwave occultation data and performance analysis based on end-to-end simulations," *J. Geophys. Res. Atmos.*, Vol. 116, No. D10, D10301, May 2011.
4. Proschek, V., G. Kirchengast, and S. Schweitzer, "Greenhouse gas profiling by infrared-laser and microwave occultation: Retrieval algorithm and demonstration results from end-to-end simulations," *Atmos. Measure. Tech. Dis.*, Vol. 4, No. 2, 2273–2328, Oct. 2011.
5. Kirchengast, G. and S. Schweitzer, "Climate benchmark profiling of greenhouse gases and thermodynamic structure and wind from space," *Geophys. Res. Lett.*, Vol. 38, No. 13, L13701, Jul. 2011.
6. Proschek, V., G. Kirchengast, C. Emde, and S. Schweitzer, "Greenhouse gas profiling by infrared-laser and microwave occultation in cloudy air: Results from end-to-end simulations," *J. Geophys. Res. Atmos.*, Vol. 119, No. 21, 12,372–12,390, 2014.
7. Pelliccia, F., F. Pacifici, S. Bonafoni, P. Basili, N. Pierdicca, P. Ciotti, and W. J. Emery, "Neural networks for arctic atmosphere sounding from radio occultation data," *IEEE Trans. Geosci. Remote Sensing*, Vol. 49, No. 12, 4846–4855, Dec. 2011.
8. Sokolovskiy, S., "Effect of super refraction on inversions of radio occultation signals in the lower troposphere," *Radio Science*, Vol. 38, No. 3, 1058, Jun. 2003.

9. Von Engeln, A. and J. Teixeira, "A ducting climatology derived from the European centre for medium-range weather forecasts global analysis fields," *J. Geophys. Res. Atmos.*, Vol. 109, No. D18, D18104, Sep. 2004.
10. Zuffada, C., G. A. Hajj, and E. R. Kursiniski, "A novel approach to atmospheric profiling with a mountain-based or airborne GPS receiver," *J. Geophys. Res. Atmos.*, Vol. 104, No. D20, 24435–24447, Oct. 1999.
11. Wang, H. G., Z. S. Wu, S. F. Kang, and Z. W. Zhao, "Monitoring the marine atmospheric refractivity profiles by ground-based GPS occultation," *IEEE Geosci. Remote Sensing Lett.*, Vol. 10, No. 4, 962–965, Jul. 2013.
12. Wu, X., X. Wang, and D. Lü, "Retrieval of vertical distribution of tropospheric refractivity through ground-based GPS observation," *Adv. Atmos. Sci.*, Vol. 31, No. 1, 37–47, Jan. 2014.
13. Lowry, A. R., C. Rocken, S. V. Sokolovskiy, and K. D. Anderson, "Vertical profiling of atmospheric refractivity from ground-based GPS," *Radio Science*, Vol. 37, No. 3, 13-1–19, Jun. 2002.
14. Geem, Z. W., "Improved harmony search from ensemble of music players," *Knowledge-based Intelligent Information and Engineering Systems*, 86–93, Springer, 2006.
15. Geem, Z. W., "Optimal cost design of water distribution networks using harmony search," *Engr. Optim.*, Vol. 38, No. 3, 259–277, 2006.
16. Bönsch, G. and E. Potulski, "Measurement of the refractive index of air and comparison with modified Edlén's formulae," *Metrologia*, Vol. 35, 133–139, 1998.
17. http://www.ecmwf.int/.
18. Anderson, G. P., S. A. Clough, F. X. Kneizys, J. H. Chetwynd, and P. Shettle, "AFGL atmospheric constituent profiles (0.120 km)," *Environm. Res. Papers*, No. 954, AFGL-TR-86-0110, Optical Physics Div., Air Force Geophys. Lab., Hanscom AFB, MA, USA, May 1986.
19. Schweitzer, S., G. Kirchengast, and V. Proschek, "Atmospheric influences on infrared-laser signals used for occultation measurements between low earth orbit satellites," *Atmos. Measure. Tech. Dis.*, Vol. 4, No. 3, 2689–2747, Oct. 2011.
20. Jacobson, M. Z., *Fundamentals of Atmospheric Modeling*, Cambridge Univ. Press, 2005.
21. Rothman, L. S., I. E. Gordon, Y. Babikov, A. Barbe, D. C. Benner, P. F. Bernath, M. Birk, L. Bizzocchi, V. Boudon, and L. R. Brown, "The HITRAN2012 molecular spectroscopic database," *J. Quantitative Spectroscopy Radiative Transfer*, Vol. 130, 4–50, 2013.
22. Ortabasi, U. and H. Friedman, "Powersphere: A photovoltaic cavity converter for wireless power transmission using high power lasers," *IEEE World Conf. Photovolt. Energy Conv.*, Vol. 1, 126–129, 2006.
23. Summerer, L. and O. Purcell, "Concepts for wireless energy transmission via laser," *Euro. Space Agency (ESA)-Adv. Concepts Team*, 2008.
24. Steinkopf, R., A. Gebhardt, S. Scheiding, et al., "Metal mirrors with excellent figure and roughness," *Int. Soc. Opt. Photon.*, Vol. 71020C, 1–20, 2008.
25. Yang, S.-H. and J.-F. Kiang, "Optimization of sparse linear arrays using harmony search algorithms," *IEEE Trans. Antennas Propagat.*, Vol. 63, No. 11, 4732–4738, Nov. 2015.
26. Ratnaweera, A., S. Halgamuge, and H. C. Watson, "Self-organizing hierarchical particle swarm optimizer with time-varying acceleration coefficients," *IEEE Trans. Evolutionary Comput.*, Vol. 8, No. 3, 240–255, Jun. 2004.
27. Jensen, A. S., M. S. Lohmann, H. H. Benzon, and A. S. Nielsen, "Full spectrum inversion of radio occultation signals," *Radio Science*, Vol. 38, No. 3, 6-1–15, May 2003.
28. Salby, M. L., *Fundamentals of Atmospheric Physics*, Academic Press, 1996.